The Value of 3 Tesla Field Strength for Musculoskeletal Magnetic Resonance Imaging

Iman Khodarahmi, MD, PhD and Jan Fritz, MD

Abstract: Musculoskeletal magnetic resonance imaging (MRI) is a careful negotiation between spatial, temporal, and contrast resolution, which builds the foundation for diagnostic performance and value. Many aspects of musculoskeletal MRI can improve the image quality and increase the acquisition speed; however, 3.0-T field strength has the highest impact within the current diagnostic range. In addition to the favorable attributes of 3.0-T field strength translating into high temporal, spatial, and contrast resolution, many 3.0-T MRI systems yield additional gains through high-performance gradients systems and radiofrequency pulse transmission technology, advanced multichannel receiver technology, and high-end surface coils. Compared with 1.5 T, 3.0-T MRI systems yield approximately 2-fold higher signal-to-noise ratios, enabling 4 times faster data acquisition or double the matrix size. Clinically, 3.0-T field strength translates into markedly higher scan efficiency, better image quality, more accurate visualization of small anatomic structures and abnormalities, and the ability to offer high-end applications, such as quantitative MRI and magnetic resonance neurography. Challenges of 3.0-T MRI include higher magnetic susceptibility, chemical shift, dielectric effects, and higher radiofrequency energy deposition, which can be managed successfully. The higher total cost of ownership of 3.0-T MRI systems can be offset by shorter musculoskeletal MRI examinations, higher-quality examinations, and utilization of advanced MRI techniques, which then can achieve higher gains and value than lower field systems. We provide a practice-focused review of the value of 3.0-T field strength for musculoskeletal MRI, practical solutions to challenges, and illustrations of a wide spectrum of gainful clinical applications.

Key Words: musculoskeletal, magnetic resonance imaging, 3.0 T, acceleration, 3D MRI, whole-body MRI, MR neurography, interventional MRI, metal artifact reduction MRI

(*Invest Radiol* 2021;56: 749–763)

Musculoskeletal magnetic resonance imaging (MRI) has evolved into a cornerstone of precision sports medicine and orthopedic surgery by providing highly accurate information for the detection, diagnosis, characterization, treatment monitoring, and surveillance of a broad variety of musculoskeletal conditions of bone, tendons, ligaments, muscles, connective tissues, and nerves.[1–3]

One of the value-defining attributes of musculoskeletal MRI that set it apart from radiography, ultrasonography, and computed tomography is the unparalleled combination of high contrast and high spatial resolution permitting differential display of submillimeter musculoskeletal structures.[4,5]

Although high diagnostic performance is a critical value component, maximizing the efficiency of musculoskeletal MRI examinations is equally important for its value. Maximized efficiency catalyzes other value demands, including increasing the availability and accessibility through increasing the number of examination slots, and improving patient tolerability by shortening exam durations, thereby reducing motion artifacts, decreasing sedation and anesthesia needs in pediatric and adult patients, improving turnaround times, and maximizing throughput to offset decreasing reimbursements.[6–8]

Many hardware and software aspects of MRI contribute to improving the image quality and maximizing the acquisition speed of musculoskeletal MRI examinations[9]; however, 3.0-T field strength may have the highest impact within the current diagnostic range. In addition to 3.0-T field strength translating into high spatial, contrast, and temporal resolutions of musculoskeletal MRI examinations, many 3.0-T MRI systems are additionally equipped with high-performance gradients systems and radiofrequency pulse transmission technology, advanced multichannel receiver technology, and high-end surface coils. The quality of transmitting and receiving components of 3.0-T MRI systems permits maximizing pulse sequence gains through improved compaction of echo trains and efficient use of parallel imaging, simultaneous multislice acceleration, compressed sensing–based undersampling, and artificial intelligence–based image reconstruction.[10,11]

The higher total cost of ownership of 3.0-T MRI systems can be offset by shorter and higher-quality musculoskeletal MRI examinations, utilization of advanced MRI techniques, and shared use with other services with similar demands, such as neuroradiology. The benefits of 3.0-T MRI often outweigh the cost for sites with sufficient daily MRI volumes.

We provide a practice-focused review of the value of 3.0-T field strength for musculoskeletal MRI, practical solutions to challenges, and illustrations of a wide spectrum of gainful clinical applications.

THE VALUE PROPOSITIONS OF 3-T MRI

Musculoskeletal MRI is a careful negotiation between spatial, temporal, and contrast resolution, which together define image quality and, ultimately, build the foundation for diagnostic performance and value.

At the center of this negotiation is the signal-to-noise ratio (SNR) yield of an MRI system, which can be considered a surrogate marker for what is colloquially referred to as "MR signal" and the most important value-defining currency of musculoskeletal MRI.

The static B_0 field strength is the primary factor for the SNR gain, which secondarily defines the practically attainable spatial, temporal, and contrast resolution and tertiarily image quality, efficiency, and application diversity (Fig. 1).

Compared with 1.5 T, 3.0-T MRI systems yield an approximately 2-fold higher SNR,[12] permitting smaller variations based on generational differences of magnet design, gradient and radiofrequency coil performance, signal conversion, multichannel technology, and surface coils (Fig. 2).

The 2-fold SNR gain of 3.0 T has the highest impact on the temporal resolution. Three-Tesla field strength enables 4 times faster data acquisition to obtain the same SNR than 1.5 T while keeping spatial resolution and other sequence timing-defining factors constant. As there is a square root relationship between SNR and the number of excitations according to $SNR \sim \sqrt{NEX}$, doubling the SNR requires quadrupling the number of acquisitions. This relationship can also be expressed as $B_0 \sim \frac{1}{\sqrt{t}}$. Practically, the 3.0-T SNR gain permits more effective utilization

Received for publication April 19, 2021; and accepted for publication, after revision, May 2, 2021.

From the Division of Musculoskeletal Radiology, Department of Radiology, NYU Grossman School of Medicine, New York, NY.

Conflicts of interest and sources of funding: J.F. received institutional research support from Siemens AG, BTG International, Zimmer Biomet, DePuy Synthes, QED, and SyntheticMR; is a scientific advisor for Siemens AG, SyntheticMR, GE Healthcare, QED, BTG International, ImageBiopsy Lab, Boston Scientific, and Mirata Pharmaceuticals; and has shared patents with Siemens Healthcare and Johns Hopkins University. I.K. has nothing to disclose.

Correspondence to: Jan Fritz, MD, Division of Musculoskeletal Radiology, Department of Radiology, NYU Grossman School of Medicine, Rm 313, 3rd Floor, 660 1st Ave, New York, NY 10016. E-mail: jan.fritz@nyulangone.org.

ISSN: 0020-9996/21/5611–0749
DOI: 10.1097/RLI.0000000000000801

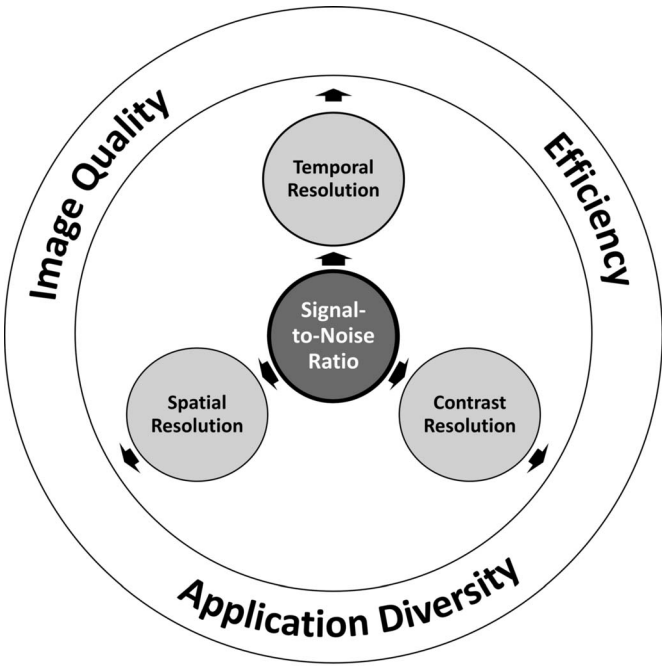

FIGURE 1. Relationship of the signal-to-noise ratio (SNR) of the 3.0-T magnetic resonance imaging (MRI) with temporal, spatial, and contrast resolution, as well as image quality, efficiency, and application diversity.

of acceleration techniques for markedly faster acquisition of 2-dimensional (2D) and 3-dimensional (3D) pulses sequences.[10,11]

The second-highest impact of the 2-fold SNR gain of 3.0 T is on the spatial resolution. Two-fold higher SNR typically permits doubling a 2D matrix size to obtain the same SNR as 1.5 T while keeping other SNR-defining factors constant. This gain is based on a square root relationship of the SNR difference between the ratio of two 2D matrix sizes according to $SNR \sim \sqrt{(original\ matrix\ size/new\ matrix\ size)}$. Practically, doubling a 2D matrix size requires twice the original SNR, which means doubling the in-plane resolution of 2D MRI scans at 3.0 T should result in similar SNR as 1.5-T MRI scans. Similarly, the SNR gain may be translated into thinner slice acquisitions at 3.0 T.

In addition to the 3-T SNR gains enabling approximately 4 times faster image acquisitions or 2-fold higher matrix resolution than 1.5 T, the contrast resolution of musculoskeletal tissues is often higher on 3.0-T MRI. The combination of higher SNR at 3.0 T and inherent modulation of musculoskeletal T1 and T2 constants result in a wider separation of the T1 recovery and T2 decay curves and visually improved tissue contrasts (Fig. 2).

PULSE SEQUENCE PARAMETER SELECTION

The field strength–dependent differences of T1 and T2 constants of synovial fluid, subcutaneous fat and fatty marrow, articular cartilage, skeletal muscle, menisci, ligaments, and tendons should be considered for optimal signal gain and contrast when designing musculoskeletal 3.0-T MRI protocols.

At 3.0 T, the T1 constants of musculoskeletal tissues are approximately 20% longer, whereas the corresponding T2 constants are approximately 15% shorter than at 1.5 T.[13] Thus, the longitudinal magnetizations of fluid and articular cartilage need more time to recover sufficiently, whereas the transverse magnetization decays faster.

Fast and turbo spin echo (TSE) pulse sequences serve as good examples of how T1 and T2 differences translate to clinical protocol differences due to their versatility, including the ability to sample T1, proton density, intermediate, and T2 contrasts for differentiation of musculoskeletal tissues and characterization of a broad spectrum of conditions; utilization of various fat suppression techniques, including spectrally selective suppression pulses, Dixon techniques, water exaction techniques, and short tau inversion recovery (STIR); high signal gains with optimized repetition time, echo time, echo train lengths, and inter–echo spacing; the ability for high spatial resolution, acceleration with parallel imaging, simultaneous multislice acquisition, and compressed sensing–based undersampling; and ability to accommodate 2D and 3D acquisition schemes, quantitative imaging, diffusion-weighted imaging, and advanced metal artifact suppression techniques.[14,15]

Practically, T1 and T2 differences are most impactful for optimizing the fluid brightness and articular cartilage contrast on native intermediate-weighted, proton density–weighted, and T2-weighted TSE pulse sequences. The use of optimal repetition and echo time is foundational for (*a*) maximizing SNR gain, (*b*) improving the detection and characterization of anatomical structures and abnormalities associated with fluid-bright edema, inflammation, and fluid, and (*c*) optimizing the display and differentiation of musculoskeletal tissues with inherently low concentrations of protons, long T1, and short T2, including ligaments, tendons, fibrocartilage, and also articular cartilage.[16]

When designing intermediate-weighted, proton density–weighted, and T2-weighted pulse sequences for clinical musculoskeletal 3.0-T MRI protocols, an important consideration is that the cross-over point of fat

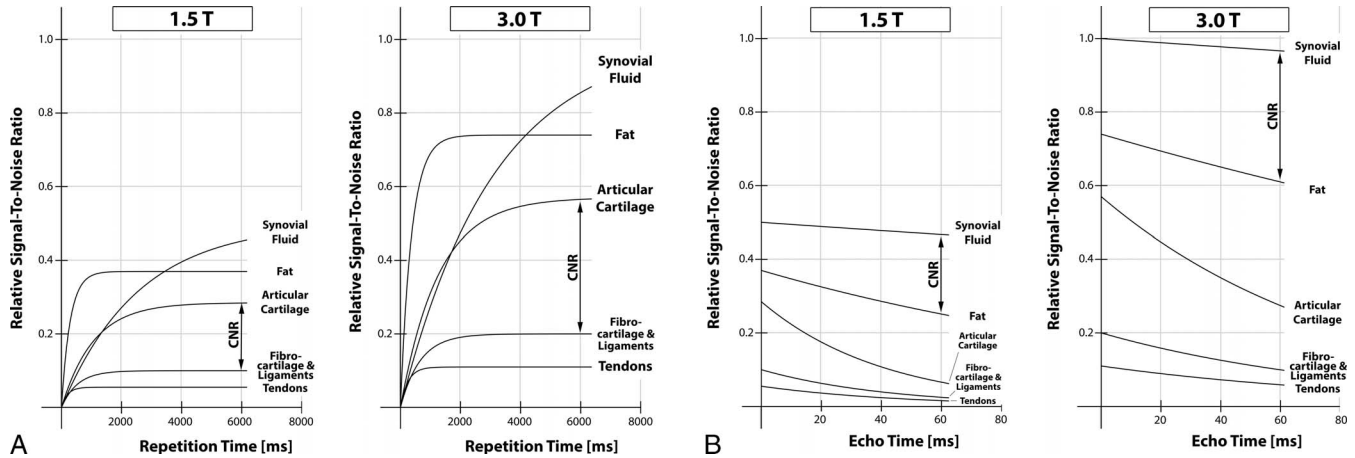

FIGURE 2. T1 constants (A) and T2 constants (B) of musculoskeletal tissues at 1.5 T and 3.0 T with associated signal-to-noise ratio (SNR) and contrast to noise ratio (CNR) differences. Compared with 1.5 T, 3.0 T yields approximately twice the SNR and higher CNR, defined as the *y* axis difference of 2 musculoskeletal tissues.

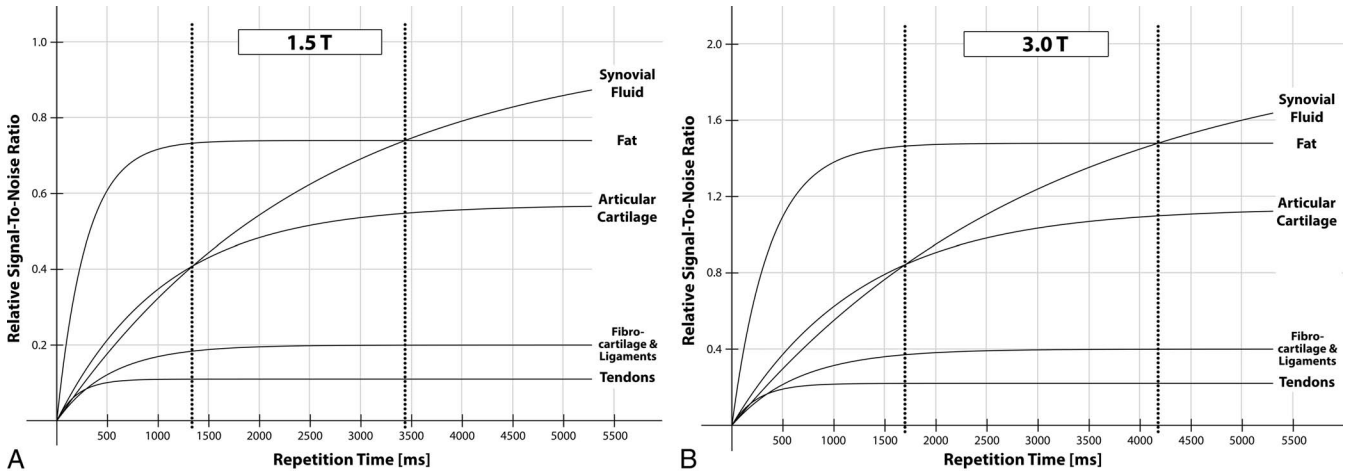

FIGURE 3. T1 constants of musculoskeletal tissues at 1.5 T (A) and 3.0 T (B) using normalized relative signal intensities (*y* axes) for comparison purposes. The 3.0-T T1 constants of musculoskeletal tissues (B) are approximately 20% longer than at 1.5 T (A), which is exemplified by the later occurring cross-over points of synovial fluid and articular cartilage (left dotted lines in A and B), and synovial fluid and fat (right dotted lines in A and B) at 3.0 T. Note the different y-axes scales indicating approximately 2-fold higher signal-to-noise ratios of 3.0 T (B) than 1.5T (A).

and synovial fluid occurs 600 to 700 milliseconds later, at approximately 4200 milliseconds when compared with 1.5 T (Fig. 3). As such, 3.0-T pulse sequences require longer repetition times to recover the longitudinal magnetization of fluid and articular cartilage sufficiently. Similarly, as T2 constants are shorter, shorter effective echo times should be used for 3.0-T protocols to optimize tissue contrast and maximizing the signal gain. However, the effective echo time differences are smaller and range typically between 5 and 10 milliseconds.

For proton density–weighted and intermediate-weighted pulse sequences, repetition times of ≥4000 milliseconds and intermediate echo times of 30 to 35 milliseconds are optimal for fluid sensitivity, zonal display of articular cartilage layers, and maximizing the signal gain (Fig. 4). With repetition times below 2500 milliseconds, the recovery of the T1 constants of synovial fluid is typically insufficient and may result in dark fluid, which may render MRI scans insensitive for structural injuries, such as ligamentous disruption, fibrocartilage tears, and articular cartilage defects.

For T2-weighted MRI scans without and with fat suppression, the use of repetition times greater than 3800 milliseconds and echo time approximately 60 milliseconds achieves high fluid specificity. Longer echo times will further increase fluid specificity but sacrifice the signal and differential contrast of other tissues. Effective echo times of 60 to 70 milliseconds additionally eliminate relevant magic angle effects.[17]

The time needed for longer repetition times can be compensated for with longer echo trains, echo spacing–shortening higher receiver bandwidths, and acceleration techniques, such as partial phase Fourier sampling, parallel imaging undersampling, simultaneous multislice acquisition, and compressed sensing–based undersampling.[10,11]

Fluid brightness can also be improved through driven equilibrium techniques, which accelerate spin recovery.[18] However, driven

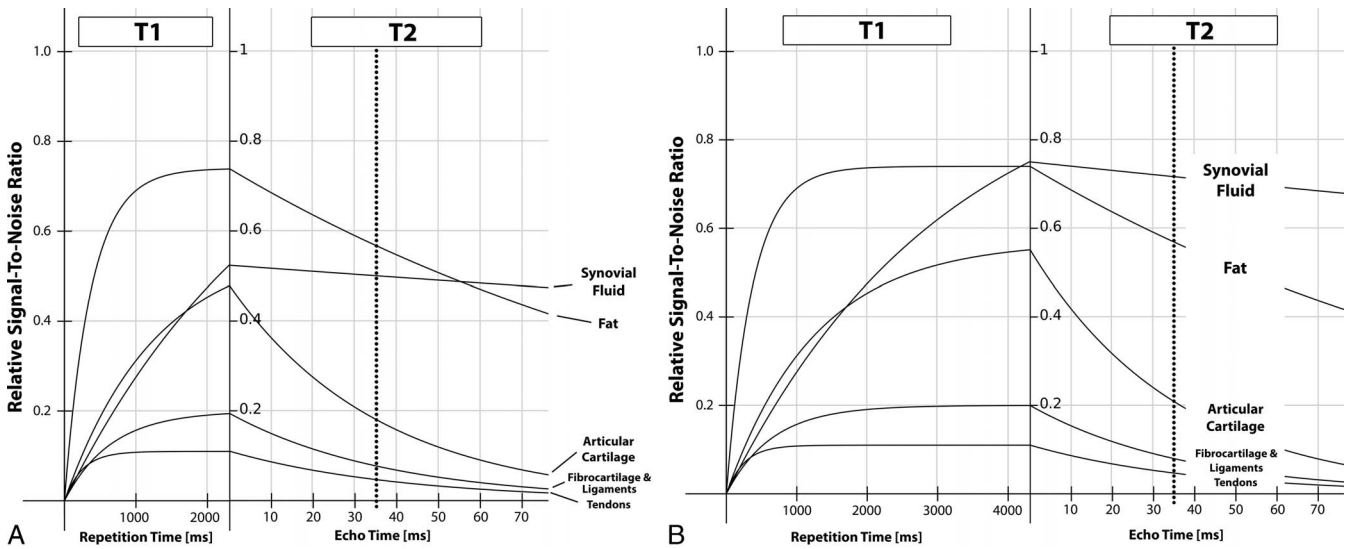

FIGURE 4. Proton density-weighted pulse sequence timings based on different repetition times at 3.0-T field strength demonstrating effects of longer T1 constants of musculoskeletal tissues at 3.0-T MRI. A, Proton density-weighted pulse sequence with a short repetition time of 2500 milliseconds and echo time of 35 milliseconds results in darker fluid than fat intensity due to insufficient recovery of longitudinal magnetization, which may render MRI scans insensitive for structural injuries, such as ligamentous disruption, fibrocartilage tears, and articular cartilage defects. B, Proton density-weighted pulse sequence with a longer repetition time of 4300 milliseconds and an echo time of 35 milliseconds results in synovial fluid having the highest signal intensity above that of fat tissues due to appropriate recovery of the longitudinal magnetization.

equilibrium pulses may reduce the overall SNR by up to 10% and may reduce the contrast resolution of articular cartilage, muscle, fibrocartilage, ligaments, and tendons.

Native T1-weighted MRI scans are predominantly fat sensitive, and thus, ideally suited for bone marrow analysis in the setting of osteomyelitis, neoplastic disease, and visualization of gadolinium-based contrast enhancement.[1] As the longitudinal magnetization of fatty tissues recovers slower at 3.0 T, practically, 100 to 200 millisecond longer repetition times can be used at 3.0 T.

GRADIENT AND RADIOFREQUENCY COILS

The practically achievable minimum radiofrequency pulse length, maximum gradient speed and strength, and widest receiver bandwidth are important characteristics for MRI system performance that directly determine the efficiency of musculoskeletal MRI examinations. Three-Tesla MRI systems often offer higher-performing radiofrequency coil and gradient system choices, which further count for performance differences compared with lower field strength MRI systems.

Although often not included in equations for pulse sequence acquisition times, faster excitation and refocusing radiofrequency pulses occupy less time within pulse sequences and substantially increase acquisition speed.[10]

Similarly, fast and strong gradients require less time to prepare and carry out encoding steps, resulting in faster pulse sequence acquisitions. Gradient speed indicates how fast gradient fields can reach the requested value (slew rate, [T/m/s]), whereas gradient strength (mT/m) determines how quick gradients can achieve their intended effects. Current clinical 3.0-T scanners have gradients with slew rates of approximately 200 T/m/s and gradient strengths of approximately 60 to 80 mT/m.

High-performance gradients also permit faster sampling of the MRI signal at high receiver bandwidths, which reduces chemical shift artifacts and improves edge sharpness. The resulting shorter inter–echo spacing additionally may further shorten pulse sequence durations.[12] Doubling the receiver bandwidth offsets the 3.0-T SNR gain by approximately 30%. However, optimized repetition and echo times limit the SNR loss to approximately 18% or less.[19,20] In addition, the resulting shorter echo spacing affords better tissue contrast, decreased susceptibility artifacts, less blurring, faster acquisitions, and sampling of earlier echoes with higher signal.

CHALLENGES AND SOLUTIONS OF MUSCULOSKELETAL MRI AT 3.0 T

Susceptibility Artifacts

Microscopic variations in the magnetic field that occur near the interfaces of materials of different magnetic susceptibility, such as the air-tissue interface of the paranasal sinuses, result in susceptibility artifacts. These artifacts are proportional to the static magnetic field strength and, therefore, higher at 3.0 T. The same effect results in shorter T2* values at 3.0 T.[21]

Except for orthopedic implants, which we discuss below, such artifacts are of less concern in musculoskeletal MRI. First, B_0 shimming can be performed more effectively for smaller musculoskeletal body parts, such as joints, than larger body parts, such as the abdomen. Second, interfaces with significantly different magnetic susceptibilities are less common in musculoskeletal MRI. Moreover, spin echo–based sequences are less affected by susceptibility artifacts. One caveat here is diffusion-weighted imaging, which may be more distorted at 3.0 T when performed with gradient echo–based techniques,[22] but can be successfully addressed by employing parallel imaging, which allows for imaging at shorter echo times.[23]

Chemical Shift Artifacts

Type 1 chemical shift artifacts refer to the signal displacement along the frequency encoding direction due to the different precession frequencies of fat and water. Because precession frequencies are linearly proportional to the field strengths, type 1 in-plane chemical shift artifacts double when moving from 1.5 T to 3.0 T and are compensated for by using twice the receiver bandwidth for non–fat-suppressed pulse sequences.[19] At 7.0 T, type 1 chemical shift artifacts are markedly more pronounced manifesting in-plane and through-plane directions but can be successfully compensated for with the use of matched and increased excitation and refocusing radiofrequency pulse bandwidths.[24]

Type 2 chemical shift artifacts are intravoxel signal cancellations of fat and water protons at echo times when fat and water protons are at opposite phases. Although occurring at different echo times, type 2 chemical shift–related India ink artifacts do not increase at 3.0 T.[21]

Dielectric Artifact

Dielectric or standing wave artifacts are referred to abnormal bright and dark areas due to B_1 field inhomogeneity at higher field strength. Depending on its dielectric properties, a body region can serve as a radiofrequency resonator, in which case constructive and destructive B_1 interferences can occur with a spatial distribution depending on body part geometry and radiofrequency pulse wavelength.

The radiofrequency pulse wavelength at 1.5 T is 52 cm, which is typically larger than the axial dimensions of the human torso. With increased Larmor frequency at 3.0 T, the tissue dielectric constants increase, and the radiofrequency pulse wavelength decreases to 26 cm, approaching the axial torso dimensions. As a result, both constructive and destructive areas fall within the imaged region, causing regions of high and low signal intensity.

Dielectric effects are rare at musculoskeletal 3.0-T MRI due to the mismatch of small peripheral joints and radiofrequency wavelength. For rare occurrences in the pelvis, dielectric pads placed next to the patient can be used for correction. However, modern 3.0-T scanner systems are equipped with independent transmit channels and radiofrequency shimming capabilities, essentially eliminating this artifact for MSK MRI.[25]

Magic Angle Effect

The magic angle effect occurs with short echo time acquisitions in tissues with anisotropic structural patterns, such as tendons and cartilage. When water molecules are preferentially aligned at a 55-degree angle to the static magnetic field, decreased dipole-dipole interaction results in T2 prolongation.[17] This effect is expected to magnify at 3.0 T, although in our experience, it rarely represents a diagnostic challenge beyond what is encountered at 1.5 T.[19] The magic angle effects decrease substantially with TSE pulse sequences using echo times greater than 60 to 70 milliseconds.

Safety Considerations

Any pulse sequence and acceleration technique should be executed within mandated specific absorption rate (SAR) limits.[26] Three-Tesla pulse sequences often use higher-energy radiofrequency pulses, which impart more energy and reach SAR limits faster than 1.5 T.

Specific absorption rate management at 3.0 T includes using lower refocusing angles, lower-energy flip angle designs, longer repetition time, shorter echo train length, and reducing the number of slices.[27] For minimizing the SAR, reducing the refocusing angle is a reasonable choice, as the flip angle has a quadratic effect on SAR. Practically, reducing conventional refocusing angles as low as 120 degrees often has often little influence on perceptible image quality.

MUSCULOSKELETAL APPLICATIONS OF 3.0-T MRI

Large Joint Magnetic Resonance Imaging

Depending on how the SNR gain of 3.0 T is applied (Fig. 1), 3.0-T MRI facilitates high spatial and contrast visualization of anatomic large

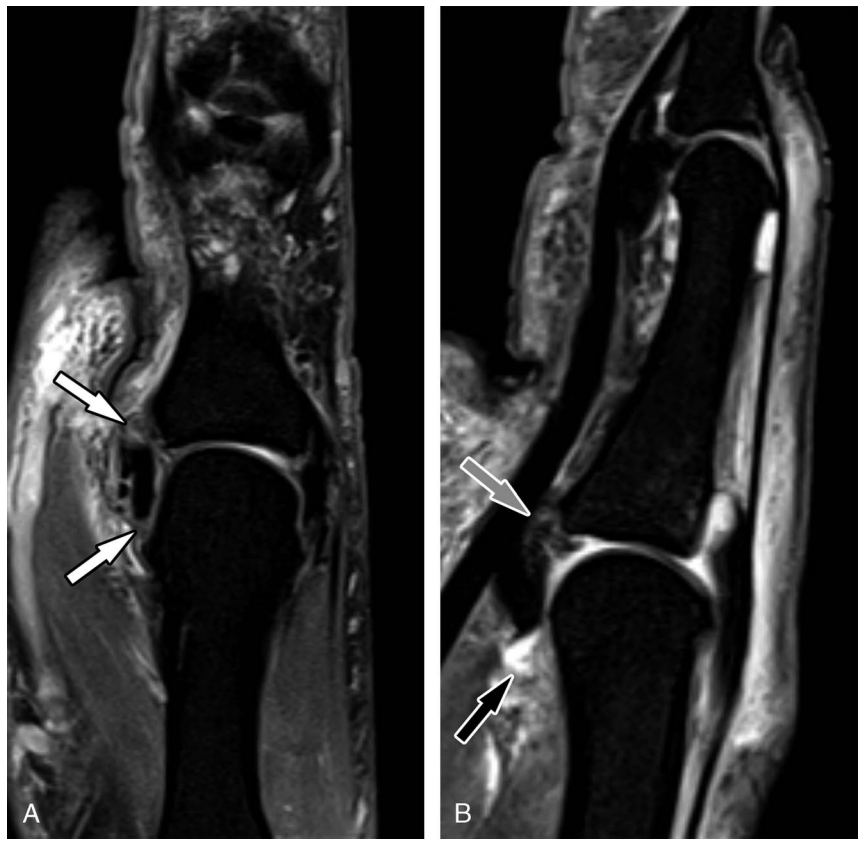

FIGURE 5. A 28-year-old man with an acute thumb injury sustained during playing American football. A, Coronal oblique T2-weighted 3.0-T MRI scan with SPAIR fat suppression (repetition time, 4300 milliseconds; echo time, 61 milliseconds; voxel size, 0.3 × 0.3 × 2.0 mm) demonstrates nondisplaced full-thickness tears (arrows) of the proximal and distal attachments of the ulnar collateral ligament of the metacarpophalangeal joint of the thumb. There is no Stener lesion. B, Sagittal oblique T2-weighted 3.0-T MRI scan with SPAIR fat suppression (repetition time, 4100 milliseconds; echo time, 58 milliseconds; voxel size, 0.3 × 0.3 × 2.0 mm) demonstrates a partial-thickness tear (gray arrow) of the volar plate of the metacarpophalangeal joint of the thumb, and partial tear of the proximal volar aspect of the joint capsule (black arrow). The MRI scans were obtained with a commercial 3.0-T MRI system (slew rate, 200 T/m/s; gradient strength, 60 mT/m) and a dedicated 16 receiver channels wrist coil.

joint structures routinely at 400 μm and less for exquisite visualization of fine anatomical detail.

Although not uniform, multiple studies show that 3.0-T advantages translate into superior diagnostic performance for detecting small lesions, such as partial-thickness cartilage defects and partial-thickness rotator cuff tendon tears.

A knee MRI meta-analysis found a 70% specificity and 85% sensitivity for 3.0-T MRI detection of articular cartilage lesions and an overall higher diagnostic effectiveness than 1.5-T MRI.[28] The diagnostic performances of 1.5-T and 3.0-T MRI were similar for ligamentous and meniscal lesions. Similarly, a study comparing combined simultaneous multislice parallel imaging–accelerated 5-minute 1.5-T and 5-minute 3.0-T knee MRI protocols that differed in spatial resolution only found higher 3.0-T detection rates for partial-thickness articular cartilage defects, whereas the detection rates for meniscal and ligamentous tears were similar.[29]

Three-Tesla MRI and 1.5-T magnetic resonance arthrography (MRA) have similarly high detection rates for acetabular labrum tears; however, 3.0-T MRI is superior to 1.5-T MRA for diagnosing acetabular cartilage defects.[30,31]

Three-Tesla MRI perform better than 1.5-T MRI and MRA for detecting glenoid labral tears, as well as partial-thickness rotator cuff tears. Based on meta-analyses, 3.0-T MRI has an 80% sensitivity and 90% to 99% specificity for detecting labral and rotator cuff tears.[32,33]

Small Joint Magnetic Resonance Imaging

Three Tesla is ideal for evaluating the delicate ligamentous structures and thin articular cartilage layers of small extremity joints (Fig. 5),[34,35] whereas the detectability of larger abnormalities, such as bone marrow edema, nondisplaced fractures, and osteomyelitis, may be similar between 1.5 T and 3.0 T.[36]

Three-Tesla MRI of the wrist has significantly higher SNR, higher contrast-to-noise ratios, and superior visibility of anatomic structures than 1.5-T systems.[37,38] In a 2007 study, 3.0-T MRI had higher interobserver agreement than 1.5 T for detecting wrist articular cartilage abnormalities,[39] although the diagnostic performances were similar, which may relate to the absence of a dedicated 3.0-T wrist coil. Three-Tesla MRI has higher diagnostic performance for diagnosing tears of the triangular fibrocartilage complex and scapholunate interosseous ligament (Fig. 6).[12,40]

Acceleration Techniques

The SNR surplus and use of high-quality multichannel receiver array coils render 3.0 T ideally suited for parallel imaging acceleration of 2D and 3D pulse sequences, including TSE pulse sequences.[41] Two-fold or 3-fold accelerations can be achieved by only sampling every second or third line in k-space, respectively.

Simultaneous multislice acquisitions excite several slices of a stack at the same time,[42] rather than successively as with conventional

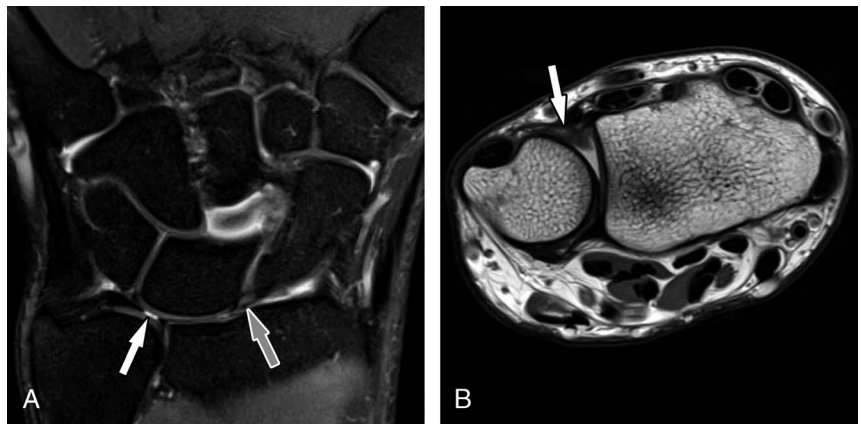

FIGURE 6. A 44-year-old man with intermittent proximal wrist pain after remote wrist trauma. A, Coronal T2-weighted 3.0-T MRI scan with SPAIR fat suppression (repetition time, 4180 milliseconds; echo time, 61 milliseconds; voxel size, 0.3 × 0.4 × 2.2 mm) of the wrist shows a central full-thickness tear (white arrow) of the triangular fibrocartilage disc and a scar-remodeled, but continuous scapholunate ligament (gray arrow). B, Axial proton density–weighted 3.0-T MRI scan (repetition time, 4450 milliseconds; echo time, 31 milliseconds; voxel size, 0.3 × 0.43 × 2.5 mm) demonstrates a scar-remodeled partial-thickness tear (arrow) of the dorsal distal radioulnar ligament. The MRI scans were obtained with a commercial 3.0-T MRI system (slew rate, 200 T/m/s; gradient strength, 60 mT/m) and a dedicated 16 receiver channels wrist coil.

techniques.[43] The multislice signal can be deconvoluted based on coil sensitivity profiles of multichannel array coils, controlled aliasing in parallel imaging results in higher acceleration (CAIPIRINHA), and field of view shifting.[44] Simultaneous multislice acquisition techniques can be applied to various pulse sequences, including 2D diffusion-weighted imaging[45–47] and 2D TSE pulse sequences.[48]

Modern blipped simultaneous multislice acquisition techniques are nearly signal neutral because of the sole signal-to-noise reduction dependency on g-factor loss.[49] Dedicated radiofrequency pulse designs,[50] lower flip angles, peripheral joint location, and local transmit coils are important factors to manage higher SAR values, as multiple slices are excited at the same time.

Efficiency gains of simultaneous multislice acquisition are based on acquiring more slices during each repetition time, effectively reducing the required minimum total repetition time to complete a pulse sequence or excess of repetition time once simultaneous multislice acquisition is added.[9,48]

Practically, the simultaneous multislice acceleration factor can be traded for concatenations, which results in a directly proportional reduction of acquisition time. Other options include the time-neutral use

TABLE 1. Four-Fold-Accelerated 3.0-T Knee MRI Protocol Using Combined Simultaneous Multislice and Parallel Imaging

Pulse Sequence Parameters	Sagittal PD TSE	Sagittal T2FS TSE	Axial PDFS TSE	Coronal PD TSE	Coronal PDFS TSE
Repetition time, ms	4000	3700	3600	4000	4000
Echo time, ms	23	56	57	23	35
Fat suppression	—	SPAIR	SPAIR	—	SPAIR
PI acceleration factor	2	2	2	2	2
SMS acceleration factor	2	2	2	2	2
FOV shift	4	4	2	4	4
Echo train length	11	11	11	4	7
Bandwidth, Hz/px	354	299	296	358	298
Echo spacing, ms	7.5	8.0	7.1	7.5	7.1
Radiofrequency pulse type	Fast	Fast	Fast	Fast	Fast
Gradient mode	Performance	Performance	Performance	Performance	Performance
Field of view, mm^2	140 × 140	140 × 140	140 × 140	140 × 140	140 × 140
Matrix frequency resolution	336	304	272	336	272
Matrix phase resolution	75%	75%	75%	75%	75%
Slice thickness, mm	3.0	3.0	3.0	3.0	3.0
Distance factor	10%	10%	10%	10%	10%
Slices	38	38	38	36	36
Phase direction	Head-to-foot	Head-to-foot	Right-to-left	Head-to-foot	Head-to-foot
Flip angle, degree	125	125	125	125	125
Phase oversampling	39%	83%	38%	39%	94%
Acquisition time, min:s	01:17	01:23	01:00	01:16	01:24

MRI, magnetic resonance imaging; PD, proton density weighting; T2, T2 weighting; T1, T1 weighting; FS, fat suppression; SPAIR, spectral attenuated inversion recovery; PI, parallel imaging; SMS, simultaneous multislice acquisition; TSE, turbo spin echo.

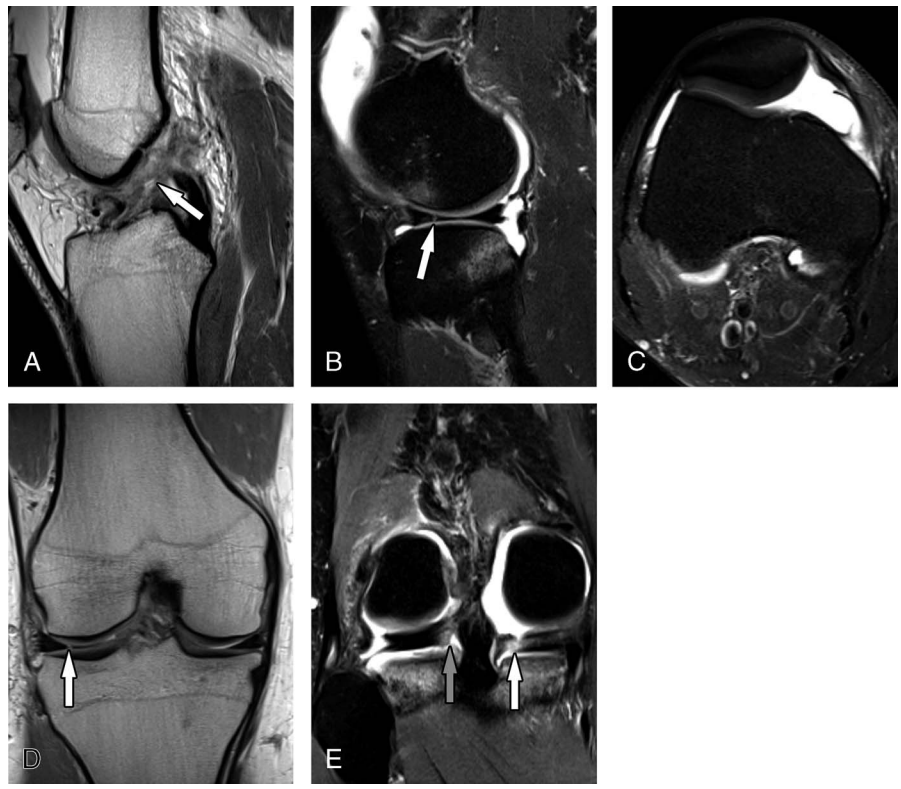

FIGURE 7. A 29-year-old man with an acute basketball injury of the right knee. Four-fold–accelerated 3.0-T knee MRI with combined simultaneous multislice and parallel imaging acceleration as shown in Table 1. A, Sagittal proton density–weighted MRI scan demonstrates a full-thickness anterior cruciate ligament tear (arrow). B, Sagittal T2-weighted MRI scan with fat suppression demonstrates a vertical tear (arrow) of the lateral meniscus with pivot shift-type bone marrow edema contusion pattern. C, Axial proton density–weighted MRI scan with fat suppression demonstrates a joint effusion and intact patellofemoral cartilage. D, Coronal proton density–weighted MRI scan demonstrates a vertical tear (arrow) of the lateral meniscus. E, Coronal T2-weighted MRI scan with fat suppression demonstrates posterior root tears of the medial (white arrow) and lateral (gray arrow) menisci. The MRI scans were obtained with a commercial 3.0-T MRI system (slew rate, 200 T/m/s; gradient strength, 60 mT/m) and a dedicated 1-transmit 18 receiver channels knee coil.

of spectrally adiabatic inversion recovery (SPAIR) fat suppression (Table 1), longer echo trains, a time-neutral increase of the number of slices, or the use of thinner slices while keeping the anatomical coverage constant.

Simultaneous multislice and parallel imaging acceleration have synergistic effects because simultaneous multislice acceleration is near signal neutral but increases SAR, whereas parallel imaging results in the signal loss but similar SAR[48] (Fig. 7).

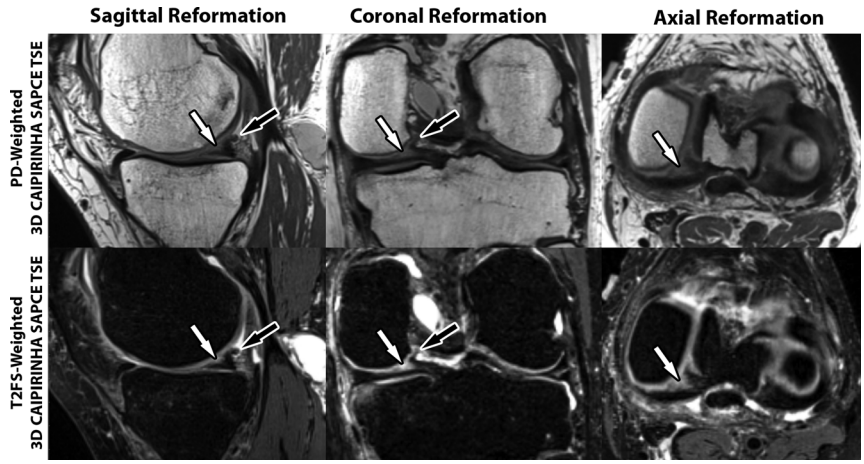

FIGURE 8. A 62-year-old man with chronic knee pain. Four-fold–accelerated 10-minute 3.0-T 3D isotropic knee MRI using proton density–weighted and fat-suppressed T2-weighted 3D CAIPIRINHA SPACE TSE pulse sequences. Sagittal, coronal, and axial MR reformation images demonstrate a degenerated, partial-thickness medial meniscus tear (white arrows) of the posterior segment with a small displaced fragment (black arrows). The MRI scans were obtained with a commercial 3.0-T MRI system (slew rate, 200 T/m/s; gradient strength, 45 mT/m) and a dedicated 1-transmit 15 receiver channels knee coil.

Combined simultaneous multislice and parallel imaging acquisitions facilitate 4-fold–accelerated 5-minute knee MRI consisting of 5 pulse sequences with different image contrasts and plane orientations equivalent to 2-fold 10-minute parallel imaging–accelerated knee MRI.[29]

Compressed sensing acceleration commonly refers to the combination of undersampling of sparse k-space regions and dedicated image reconstruction algorithms that recover missing data.[51,52]

For musculoskeletal MRI, compressed sensing–based undersampling with iterative image reconstruction can achieve faster data acquisition and retain more SNR than parallel imaging acceleration when applied to advanced metal artifact reduction,[53–55] dynamic contrast enhancement angiography,[56] and 3D pulse sequences.[57]

In practice, compressed sensing slice encoding for metal artifact correction (SEMAC) TSE affords 8-fold–accelerated metal artifact reduction of MRI of hip,[58,59] knee,[60] and ankle[61–63] arthroplasty implants, whereas parallel imaging–accelerated SEMEC is usually limited to a factor of 3.[64–67] Compressed sensing acceleration with elliptical scanning enable 60% to 70% faster SEMAC acquisitions.[58,60–62,68]

FIGURE 9. A 72-year-old man with a history of myxoid liposarcoma. A, Coronal STIR 3.0-T whole-body MRI scan shows multiple liposarcoma osseous metastases (arrows) of the pelvis and spine. B, Sagittal contrast-enhanced fat-suppressed T1-weighted 3.0-T whole-body MRI scan shows multiple enhancing liposarcoma osseous metastases (arrows) of the spine. The MRI scans were obtained with a commercial 3.0-T MRI system (slew rate, 200 T/m/s; gradient strength, 45 mT/m) using body matrix surface and spine coil arrays. Case courtesy of Prof Dr Marius Horger, Eberhardt Karls University, Tübingen, Germany.

Three-Dimensional Magnetic Resonance Imaging

Parallel imaging acceleration is essential for the clinical use of 3D TSE pulse sequences, such as sampling perfection with application optimized contrast using different flip-angle evolutions (SPACE).[69]

As 3D TSE pulse sequences have 2 phase encoding directions, and the acquisition time is directly proportional to the total number of bidirectional phase-encoding steps, the baseline acquisition time is much longer for musculoskeletal protocols with high isotropic spatial resolution, such as $0.5 \times 0.5 \times 0.5$ mm^3. However, because the square root of the number of phase encoding steps is proportional to the SNR, 3D TSE sequences yield an abundance of SNR and opportunity for advanced parallel imaging acceleration.

The 2 phase encoding directions render 3D pulse sequences accessible for bidirectional parallel imaging acceleration. Two-dimensional CAIPIRINHA additionally uses a shift between the 2 undersampling directions, which improves image reconstruction, noise, and aliasing artifacts.[70]

Three-dimensional TSE pulse sequences have undergone a remarkable evolution, reaching high accuracies for the diagnosis of internal derangement in children[71] and adults.[72–76] The 3D CAIPIRINHA SPACE TSE pulse sequence facilitates 4-fold–accelerated high-resolution multicontrast isotropic MRI of the knee and ankle in less than 10 minutes,[70,71,77–79] which is twice as fast as the original 3D SPACE TSE pulse sequence.[80,81] Flip angle modulation schemes produce T1-weighted, intermediate-weighted, and fat-suppressed fluid-sensitive T2-weighted contrasts for sports imaging of the knee[70,71,79,82] (Fig. 8), foot and ankle,[77,78] and tumor MRI.[83] Three-dimensional CAIPIRINHA SPACE TSE also facilitates artificial intelligence–based synthetic fat suppression.[84] Isotropic 3D data sets may also be created from 2D TSE MRI scans through superresolution reconstruction.[85]

Compressed sensing–accelerated acceleration of 3D SPACE TSE afforded an unprecedented 6-fold acceleration and recovery of enough SNR to realize 0.5-mm isotropic data acquisition of fluid-sensitive fat-suppressed T2-weighted data sets within 5 minutes of acquisition time for each sequence.[57] Compressed sensing has also been used to accelerate 3D CUBE fast spin echo.[86]

Quantitative Magnetic Resonance Imaging

Quantitative compositional analysis of musculoskeletal tissues, including T2, T2*, T1-rho relaxation times, diffusivity, and sodium content, have evolved into biomarkers for a variety of pathologic musculoskeletal processes.

In clinical practice, the long acquisition times often restrict conventional T2 mapping techniques to low resolution. However, at 3.0 T, modern T2 quantification techniques using combined parallel imaging and model-based mapping provide fast, accurate, and SAR-compliant high-resolution T2 mapping[87–90] and full-spectrum synthetic MRI.[91]

Oncologic Magnetic Resonance Imaging

Three-Tesla MRI of musculoskeletal tumors permits multiparametric anatomic and functional evaluations. The high 3.0-T SNR gain of 3D spoiled gradient echo–based sequences, such as volumetric interpolated

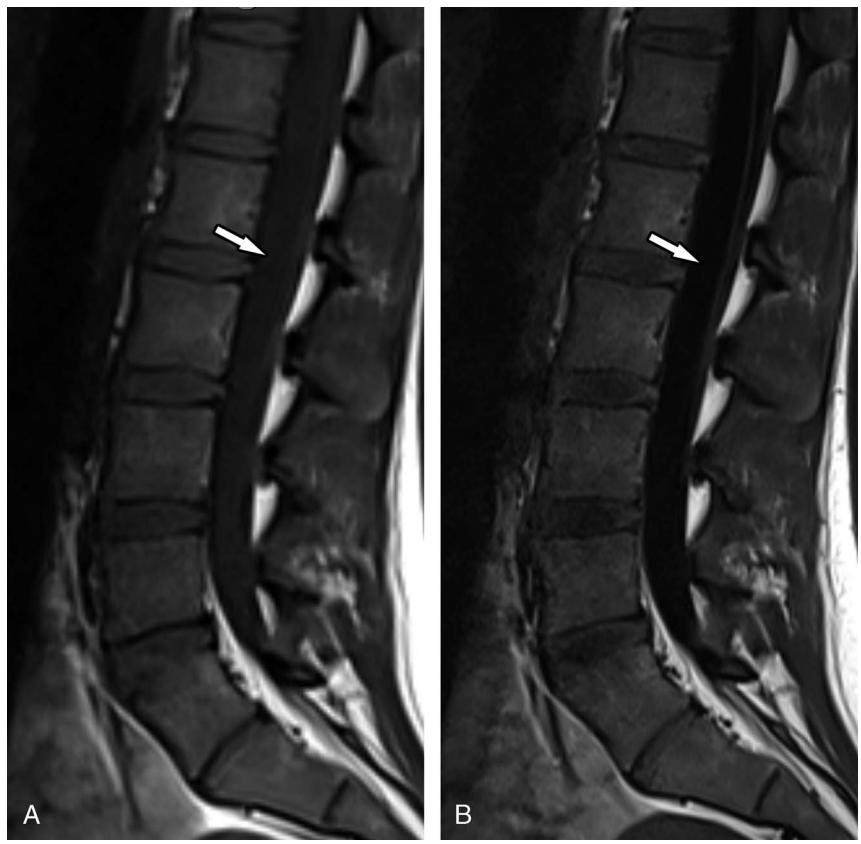

FIGURE 10. Nulling of the cerebrospinal fluid signal at 3.0 T. A, Sagittal conventional T1-weighted TSE 3.0-T MRI scan of the lumbar spine demonstrates suboptimal signal hypointensity (arrow) of the cerebrospinal fluid within the thecal sac. B, Sagittal T1-weighted TSE 3.0-T MRI scan with additional fluid-attenuated inversion recovery (FLAIR) facilitated improved signal hypointensity (arrow) of the cerebrospinal fluid within the thecal sac. Note the overall low signal intensity of the vertebral body bone marrow due to higher contents of red marrow. The MRI scans were obtained with a commercial 3.0-T MRI system (slew rate, 200 T/m/s; gradient strength, 60 mT/m) and spine coil array.

breath-hold examination (VIBE) for delayed contrast-enhanced T1-weighted acquisitions, is advantageous over conventional 2D TSE sequences due to faster acquisition with high isotropic resolution, which enables multiplanar reformation.[92]

The T1 shortening effect of gadolinium chelate–based contrast agents is unaffected by the field strength.[93,94] However, because tissues generally have longer T1 values at 3.0 T, the contrast between enhanced and unenhanced tissue is accentuated, which can be used to lower gadolinium-based contrast doses at 3.0 T.[21,95]

A valuable addition to anatomic sequences is chemical shift MRI with in-phase and opposed-phase image acquisition to differentiate bone marrow-replacing neoplasms from nonneoplastic conditions such as edematous or hematopoietic marrow. A signal drop of <20% (1.5 T) or <25% (3 T) on opposed-phase images relative to in-phase images is suggestive of neoplastic marrow replacement.[96,97] Importantly, at 3.0 T, the opposed-phase image should be acquired before the in-phase image because exaggerated susceptibility artifacts on a later acquired opposed-phase sequence may lead to an overestimation of the actual signal drop.[98]

Diffusion-weighted imaging (DWI) is a surrogate marker for tissue cellularity based on the principle that intracellular water protons are less mobile than their extracellular counterparts. Owing to inherently lower DWI signal, 3.0 T is the clinical field strength of choice.[99] Diffusion-weighted imaging and ADC mapping have been used to differentiate traumatic from pathological vertebral body fractures, differentiate benign from malignant soft tissue and bone lesions, detect tumor recurrence, and quantify treatment responses.[100]

Whole-Body Magnetic Resonance Imaging

Initially, 1.5-T MRI systems were preferred for whole-body (WB) MRI due to their lower susceptibility and dielectric artifacts[101]; however, modern 3.0-T MRI scanners permit high-resolution

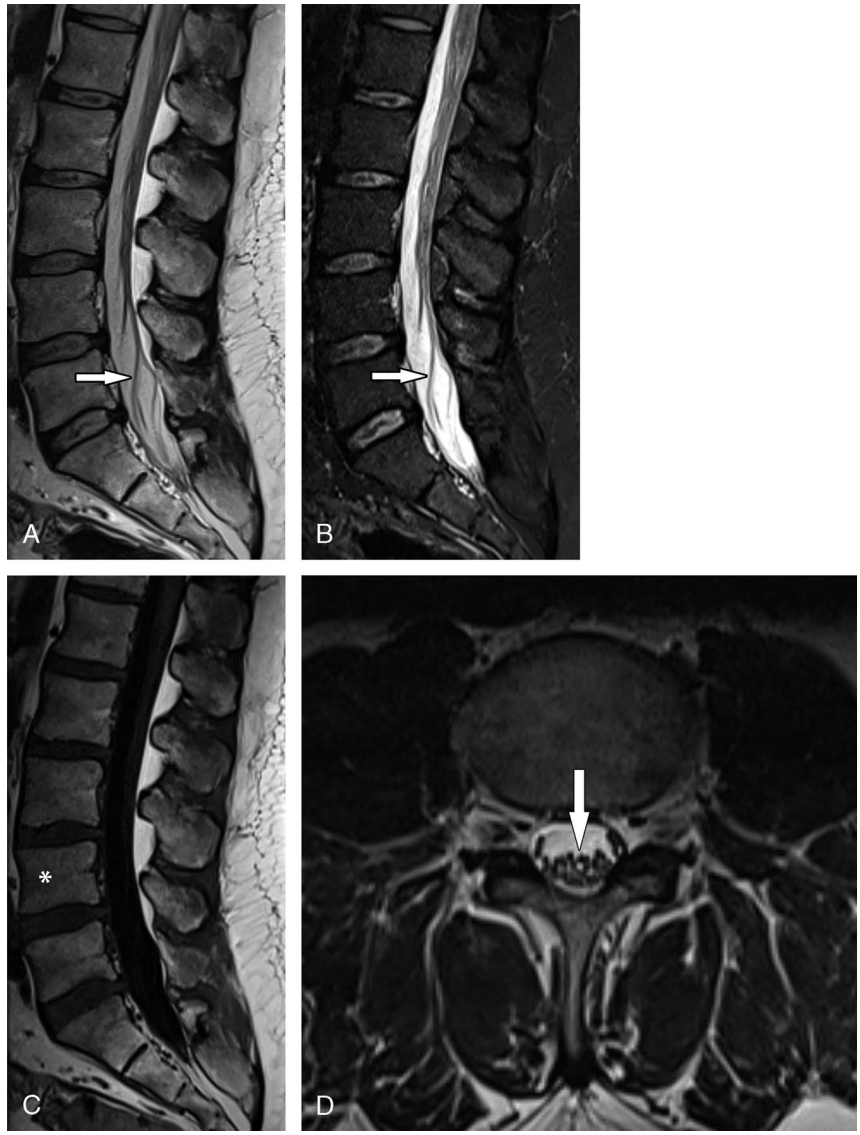

FIGURE 11. Six-minute 4-sequence 3.0-T MRI examination of the lumbar spine, including sagittal T2-weighted (A), sagittal STIR (B), sagittal T1-weighted FLAIR (C), and axial T2-weighted (D) TSE pulse sequences. The high SNRs afforded by 3.0 T translate into faster imaging acquisition and higher spatial resolution with high anatomical detail, such as the cauda equina (white arrows in A and B and D). In comparison to Figure 10, there is higher T1 signal intensity of the vertebral body bone marrow (asterisk in C) due to higher fat contents. The MRI scans were obtained with a commercial 3.0-T MRI system (slew rate, 200 T/m/s; gradient strength, 60 mT/m) and spine coil array.

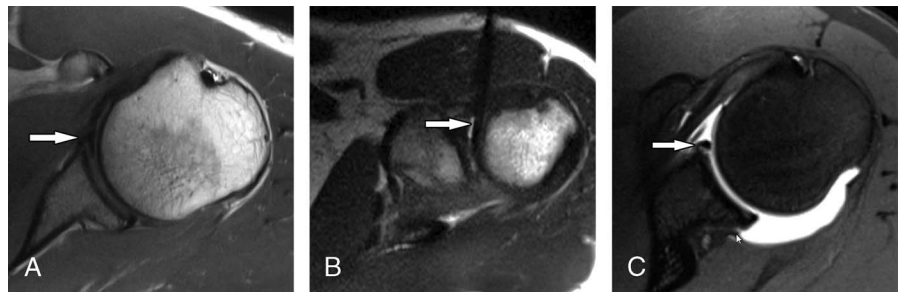

FIGURE 12. Magnetic resonance imaging–guided 3.0-T magnetic resonance arthrography of the left shoulder in a 32-year-old American football player with chronic shoulder pain. A, Diagnostic axial proton density–weighted TSE MRI scan without intra-articular contrast shows a coapted anteroinferior labrum (arrow). B, Interventional axial proton density–weighted TSE MRI scan demonstrating intra-articular glenohumeral needle puncture (arrow) through the rotator interval for intra-articular MR arthrographic injection of gadolinium-enhanced sterile saline. C, Diagnostic axial fat-suppressed T1-weighted TSE magnetic resonance arthrography image unmasks a small Perthes lesion of the anteroinferior labrum (large arrow), whereas the posterior capsular attachment is intact (small arrow). Combined diagnostic and interventional MRI were obtained with a commercial 3.0-T MRI system (slew rate, 200 T/m/s; gradient strength, 45 mT/m) and a dedicated 16 receiver channels shoulder surface coil.

multiparametric whole-body MRI in 30 to 40 minutes examination time.[102,103]

Protocol typically includes fat-sensitive sequences (T1-weighted or Dixon TSE), fluid-sensitive sequences (STIR or Dixon with water- and fat-only reconstruction), functional sequences (DWI with ADC maps), and optional contrast-enhanced fat-suppressed T1-weighted pulse sequences to detect and characterize lesions comprehensively (Fig. 9).

Whole-body MRI is established for screening, diagnosis, and surveillance of Li-Fraumeni syndrome,[104] neurofibromatosis and schwannomatosis,[102,103] multiple myeloma,[105] and chronic recurrent multifocal osteomyelitis.[106–108]

Spine Magnetic Resonance Imaging

The high spatial resolution capabilities render 3.0-T MRI ideal for evaluating fine neuroanatomical structures of the spine.[109]

Nulling of the cerebrospinal fluid signal may be incomplete at 3.0-T MRI because of longer T1 relaxation times, which can be remedied with the addition of a fluid-attenuated inversion recovery (FLAIR) pulse[110] (Fig. 10). In patients with a high fraction of red marrow components relative to fatty marrow, vertebral body bone marrow may appear darker on 3.0 T when compared with 1.5 T (Fig. 10), whereas in patients with predominantly fatty vertebral body marrow, this phenomenon is less pronounced (Fig. 11).[111]

Pulsation and flow artifacts of cerebrospinal fluid are often more pronounced on T2-weighted TSE pulse sequences but can be suppressed with head-to-foot phase encoding, saturation bands, shorter echo times concatenations, and through-plane flow compensation.[112]

Like in other body regions, isotropic 3D acquisitions of the spine can benefit from higher SNR at 3 T.[113] Fluid-sensitive gradient echo pulse sequences, such as CISS and FIESTA-C, provide high fluid signal for excellent delineation of small nerve roots. Three-dimensional TSE-based pulse sequences are less affected by susceptibility artifacts and reduce partial volume effects.[112,114] Three-dimensional dual-echo steady state has recently been shown to provide excellent delineation of small nerve roots for the cervical spine.[115]

Three-dimensional VIBE sequences at 3.0 T provide high-resolution isotropic data sets with excellent multiplanar image quality, homogeneous water excitation-based fat suppression, and reduced susceptibility to field inhomogeneities and pulsation artifacts due to short echo times. Unenhanced high-resolution VIBE images at 3 T can replace CT in the detection and characterization of pars fractures, whereas fat-suppressed contrast-enhanced VIBE data sets have better image quality and neoplastic lesion conspicuity than the T1-weighted TSE images.[116]

Magnetic Resonance Neurography

Three-Tesla MRI is preferred for magnetic resonance neurography (MRN), which refers to combined high contrast and high-resolution MRI of peripheral nerves, using 2D and 3D T1- or intermediate-weighted, fat-suppressed T2-weighted, and diffusion-weighted pulse sequences.

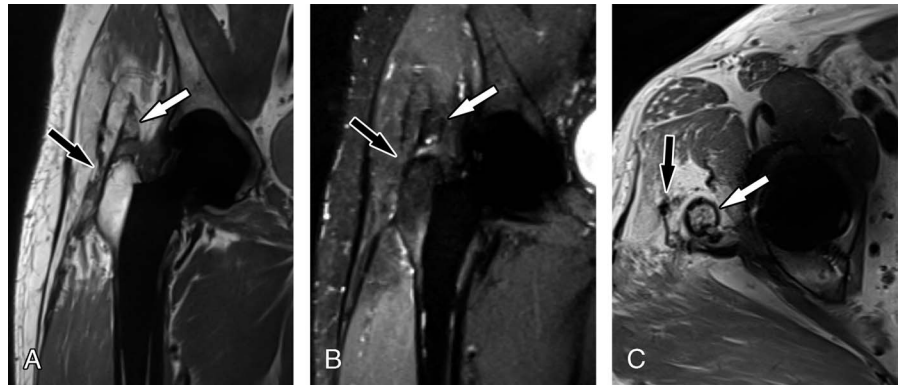

FIGURE 13. A 47-year-old man with lateral hip pain after right hip arthroplasty. Three-Tesla metal artifact reduction MRI of right hip arthroplasty implants using 8-fold compressed sensing–accelerated coronal proton density–weighted (A), coronal STIR (B), and axial proton density–weighted (C) SEMAC TSE pulse sequences show high-grade partial-thickness tearing the lateral footprint of the gluteus medius with chronically scar-remodeled and thinned tendon (black arrows), atrophy of the abductor muscle bulk, and mature heterotopic bone formation (white arrows). The MRI scans were obtained with a commercial 3.0-T MRI system (slew rate, 200 T/m/s; gradient strength, 60 mT/m) and 18 receiver channel surface and spine coil arrays.

Multiple signs of fascicular abnormality and neuropathy are more conspicuous on high-resolution 2D and 3D 3.0-T MRI scans.[117–120]

Magnetic resonance neurography at 3.0 T enables the depiction of the location, extent, cause, and character of neuropathy in various anatomic regions ranging from brachial and lumbosacral plexus to various peripheral nerves.[121,122] Compared with 1.5 T, 3.0-T MRN had superior brachial plexus visibility, although the diagnostic performances were similar.[123] Three-Tesla diffusion-weighted MRN showed superior visualization of the lumbosacral plexus but not of the brachial plexus compared with 1.5 T.[124]

In the presence of hip arthroplasty implants, lumbosacral spinal instrumentation, and pelvic osteosynthesis implants, MRN at 1.5 T may be beneficial.[125]

Interventional Magnetic Resonance Imaging

Interventional MRI has emerged as a powerful modality for procedures in which the target is poorly visible or inaccessible by other modalities in adults[126–132] and children[133–135] and to avoid exposure to ionizing radiation.[136,137] Although deep perineural injections benefit disproportionately from the high spatial resolution capabilities of 3.0-T MRI,[138–142] daily routine procedures, such as MR arthrography, can be performed in a 1-stop-shop approach as well (Fig. 12). The high spatial resolution permits intermittent or continuous anatomic localization, needle confirmation, and injection or ice ball monitoring in as little as 1 second per frame with high anatomic detail and fluid conspicuity.[143–145]

Using optimized TSE–based sequences with high receiver bandwidth and SEMAC TSE, passive visualization of MR-conditional needles and devices is practically as effective at 3.0 T than lower field strengths.[146,147]

Heating of modern MR-conditional needles for perineural, articular, and spinal injections is less of a safety concern at 3.0 T than 1.5 T using appropriate pulse sequences and parameters.[148,149]

Metal Artifact Reduction Magnetic Resonance Imaging

High-quality MRI in the presence of metal orthopedic implants may be the most challenging task at 3.0 T due to approximately 2-fold exaggerated metallic susceptibility artifacts that cause periprosthetic signal loss, signal displacement with voids and pileups, and failed spectral fat suppression.[53,55,150]

However, novel multispectral and multispatial imaging techniques can be equally effective at 3.0 T and 1.5 T[54] (Fig. 13). Direct intrasubject comparison of 1.5 T- and 3.0 T-optimized SEMAC TSE pulse sequences showed slightly larger metal artifacts of hip, knee, and ankle arthroplasty implants, but comparable diagnostic performance for a broad variety of abnormalities.[151] At 3.0 T, the combined use of parallel imaging, elliptical sampling, and compressed sensing undersampling permits 8-fold–accelerated SEMAC TSE for acquisition times of 4 to 6 minutes per pulse sequence.[58,60,62]

Modern 3.0-T MRI systems with parallel transmit capability may even be more effective to offset B_1-related artifacts than 1.5 T, which is an active area of research.[152]

The use of high-bandwidth radiofrequency pulses in the range of 4000 Hz instead of conventional 850 Hz with local transmit-receive knee coils afford substantially reduced through-plane metal artifacts, which permit using fewer SEMAC-encoding steps or omitting SEMAC for titanium-based implants.[153]

At 1.5 T and 3.0 T, metal artifact reduction MRI is routinely performed in an off-label fashion as there is no safety labeling for most implants. Although traction and rotational forces are less of a safety concern at 3.0 T with modern orthopedic implants, heating has no direct correlation with the static field strength and depends on various other factors such as implant size and radiofrequency pulse polarization.[148] A recent study of hip arthroplasty implants demonstrated overall low degrees of MRI-related heating at 3.0 T and 1.5 T, whereas heating was lower at 3.0 T than 1.5 T, suggesting a lower risk at 3.0 T.[154]

CONCLUSIONS

Musculoskeletal MRI is a careful negotiation between spatial, temporal, and contrast resolution, in which 3.0-T MRI excels with high efficiency and image quality of a broad variety of basic and advanced musculoskeletal applications that offset the higher total cost of ownership for institutions with meaningful demands for musculoskeletal MRI.

REFERENCES

1. Ahlawat S, Fritz J, Morris CD, et al. Magnetic resonance imaging biomarkers in musculoskeletal soft tissue tumors: review of conventional features and focus on nonmorphologic imaging. *J Magn Reson Imaging*. 2019;50:11–27.
2. Fritz B, Parkar AP, Cerezal L, et al. Sports imaging of team handball injuries. *Semin Musculoskelet Radiol*. 2020;24:227–245.
3. Sutter R, Stoel BC, Buck FM, et al. Internal derangements of joints-past, present, and future. *Invest Radiol*. 2015;50:601–614.
4. Coris EE, Zwygart K, Fletcher M, et al. Imaging in sports medicine: an overview. *Sports Med Arthrosc Rev*. 2009;17:2–12.
5. Hynes JP, Walsh J, Farrell TP, et al. Role of musculoskeletal radiology in modern sports medicine. *Semin Musculoskelet Radiol*. 2018;22:582–591.
6. Anzai Y, Minoshima S, Lee VS. Enhancing value of MRI: a call for action. *J Magn Reson Imaging*. 2019;49:e40–e48.
7. Link TM, Patel R. The need for short MRI examinations: a musculoskeletal perspective. *J Magn Reson Imaging*. 2019;49:e49–e50.
8. Geethanath S, Vaughan JT Jr. Accessible magnetic resonance imaging: a review. *J Magn Reson Imaging*. 2019;49:e65–e77.
9. Runge VM, Richter JK, Heverhagen JT. Speed in clinical magnetic resonance. *Invest Radiol*. 2017;52:1–17.
10. Del Grande F, Guggenberger R, Fritz J. Rapid musculoskeletal MRI in 2021: value and optimized use of widely accessible techniques. *AJR Am J Roentgenol*. 2021;216:704–717.
11. Fritz J, Guggenberger R, Del Grande F. Rapid musculoskeletal MRI in 2021: clinical application of advanced accelerated techniques. *AJR Am J Roentgenol*. 2021;216:718–733.
12. Anderson ML, Skinner JA, Felmlee JP, et al. Diagnostic comparison of 1.5 Tesla and 3.0 Tesla preoperative MRI of the wrist in patients with ulnar-sided wrist pain. *J Hand Surg Am*. 2008;33:1153–1159.
13. Gold GE, Han E, Stainsby J, et al. Musculoskeletal MRI at 3.0 T: relaxation times and image contrast. *AJR Am J Roentgenol*. 2004;183:343–351.
14. Fritz J, Lurie B, Potter HG. MR imaging of knee arthroplasty implants. *Radiographics*. 2015;35:1483–1501.
15. Fritz J, Lurie B, Miller TT, et al. MR imaging of hip arthroplasty implants. *Radiographics*. 2014;34:E106–E132.
16. Potter HG, Schachar J. High resolution noncontrast MRI of the hip. *J Magn Reson Imaging*. 2010;31:268–278.
17. Richardson ML, Amini B, Richards TL. Some new angles on the magic angle: what MSK radiologists know and don't know about this phenomenon. *Skeletal Radiol*. 2018;47:1673–1681.
18. Melhem ER, Itoh R, Folkers PJ. Cervical spine: three-dimensional fast spin-echo MR imaging—improved recovery of longitudinal magnetization with driven equilibrium pulse. *Radiology*. 2001;218:283–288.
19. Kuo R, Panchal M, Tanenbaum L, et al. 3.0 Tesla imaging of the musculoskeletal system. *J Magn Reson Imaging*. 2007;25:245–261.
20. Craig JG, Go L, Blechinger J, et al. Three-Tesla imaging of the knee: initial experience. *Skeletal Radiol*. 2005;34:453–461.
21. Chang KJ, Kamel IR, Macura KJ, et al. 3.0-T MR imaging of the abdomen: comparison with 1.5 T. *Radiographics*. 2008;28:1983–1998.
22. Rosenkrantz AB, Oei M, Babb JS, et al. Diffusion-weighted imaging of the abdomen at 3.0 Tesla: image quality and apparent diffusion coefficient reproducibility compared with 1.5 Tesla. *J Magn Reson Imaging*. 2011;33:128–135.
23. Bammer R, Keeling SL, Augustin M, et al. Improved diffusion-weighted single-shot echo-planar imaging (EPI) in stroke using sensitivity encoding (SENSE). *Magn Reson Med*. 2001;46:548–554.
24. von Deuster C, Sommer S, Germann C, et al. Controlling through-slice chemical-shift artifacts for improved non-fat-suppressed musculoskeletal turbo-spin-echo magnetic resonance imaging at 7 T. *Invest Radiol*. 2021.
25. Alizai H, Chang G, Regatte RR. MRI of the musculoskeletal system: advanced applications using high and ultrahigh field MRI. *Semin Musculoskelet Radiol*. 2015;19:363–374.
26. Allison J, Yanasak N. What MRI sequences produce the highest specific absorption rate (SAR), and is there something we should be doing to reduce the SAR during standard examinations? *AJR Am J Roentgenol*. 2015;205:W140.

27. Alsop DC. The sensitivity of low flip angle RARE imaging. *Magn Reson Med*. 1997;37:176–184.
28. Cheng Q, Zhao FC. Comparison of 1.5- and 3.0-T magnetic resonance imaging for evaluating lesions of the knee: a systematic review and meta-analysis (PRISMA-compliant article). *Medicine (Baltimore)*. 2018;97:e12401.
29. Del Grande F, Rashidi A, Luna R, et al. Five-minute five-sequence knee MRI using combined simultaneous multislice and parallel imaging acceleration: comparison with 10-minute parallel imaging knee MRI. *Radiology*. 2021;203655.
30. Chopra A, Grainger AJ, Dube B, et al. Comparative reliability and diagnostic performance of conventional 3T magnetic resonance imaging and 1.5T magnetic resonance arthrography for the evaluation of internal derangement of the hip. *Eur Radiol*. 2018;28:963–971.
31. Magee T. Comparison of 3.0-T MR vs 3.0-T MR arthrography of the hip for detection of acetabular labral tears and chondral defects in the same patient population. *Br J Radiol*. 2015;88:20140817.
32. Liu F, Cheng X, Dong J, et al. Imaging modality for measuring the presence and extent of the labral lesions of the shoulder: a systematic review and meta-analysis. *BMC Musculoskelet Disord*. 2019;20:487.
33. Liu F, Dong J, Shen WJ, et al. Detecting rotator cuff tears: a network meta-analysis of 144 diagnostic studies. *Orthop J Sports Med*. 2020;8:2325967119900356.
34. Rashidi A, Haj-Mirzaian A, Dalili D, et al. Evidence-based use of clinical examination, ultrasonography, and MRI for diagnosing ulnar collateral ligament tears of the metacarpophalangeal joint of the thumb: systematic review and meta-analysis. *Eur Radiol*. 2021.
35. Chhabra A, Soldatos T, Chalian M, et al. 3-Tesla magnetic resonance imaging evaluation of posterior tibial tendon dysfunction with relevance to clinical staging. *J Foot Ankle Surg*. 2011;50:320–328.
36. Sormaala MJ, Ruohola JP, Mattila VM, et al. Comparison of 1.5T and 3T MRI scanners in evaluation of acute bone stress in the foot. *BMC Musculoskelet Disord*. 2011;12:128.
37. Stehling C, Langer M, Bachmann R, et al. Three-Tesla magnetic resonance imaging of the wrist: diagnostic performance compared to 1.5-T. *J Comput Assist Tomogr*. 2009;33:934–939.
38. Saupe N, Prüssmann KP, Luechinger R, et al. MR imaging of the wrist: comparison between 1.5- and 3-T MR imaging—preliminary experience. *Radiology*. 2005;234:256–264.
39. Saupe N, Pfirrmann CW, Schmid MR, et al. MR imaging of cartilage in cadaveric wrists: comparison between imaging at 1.5 and 3.0 T and gross pathologic inspection. *Radiology*. 2007;243:180–187.
40. Hafezi-Nejad N, Carrino JA, Eng J, et al. Scapholunate interosseous ligament tears: diagnostic performance of 1.5T, 3T MRI, and MR arthrography—a systematic review and meta-analysis. *Acad Radiol*. 2016;23:1091–1103.
41. Deshmane A, Gulani V, Griswold MA, et al. Parallel MR imaging. *J Magn Reson Imaging*. 2012;36:55–72.
42. Larkman DJ, Hajnal JV, Herlihy AH, et al. Use of multicoil arrays for separation of signal from multiple slices simultaneously excited. *J Magn Reson Imaging*. 2001;13:313–317.
43. Hennig J, Nauerth A, Friedburg H. RARE imaging: a fast imaging method for clinical MR. *Magn Reson Med*. 1986;3:823–833.
44. Breuer FA, Blaimer M, Mueller MF, et al. Controlled aliasing in volumetric parallel imaging (2D CAIPIRINHA). *Magn Reson Med*. 2006;55:549–556.
45. Filli L, Piccirelli M, Kenkel D, et al. Simultaneous multislice echo planar imaging with blipped controlled aliasing in parallel imaging results in higher acceleration: a promising technique for accelerated diffusion tensor imaging of skeletal muscle. *Invest Radiol*. 2015;50:456–463.
46. Kenkel D, Barth BK, Piccirelli M, et al. Simultaneous multislice diffusion-weighted imaging of the kidney: a systematic analysis of image quality. *Invest Radiol*. 2017;52:163–169.
47. Phi Van VD, Becker AS, Ciritsis A, et al. Intravoxel incoherent motion analysis of abdominal organs: application of simultaneous multislice acquisition. *Invest Radiol*. 2018;53:179–185.
48. Fritz J, Fritz B, Zhang J, et al. Simultaneous multislice accelerated turbo spin echo magnetic resonance imaging: comparison and combination with in-plane parallel imaging acceleration for high-resolution magnetic resonance imaging of the knee. *Invest Radiol*. 2017;52:529–537.
49. Setsompop K, Gagoski BA, Polimeni JR, et al. Blipped-controlled aliasing in parallel imaging for simultaneous multislice echo planar imaging with reduced g-factor penalty. *Magn Reson Med*. 2012;67:1210–1224.
50. Hargreaves BA, Cunningham CH, Nishimura DG, et al. Variable-rate selective excitation for rapid MRI sequences. *Magn Reson Med*. 2004;52:590–597.
51. Runge VM, Richter JK, Heverhagen JT. Motion in magnetic resonance: new paradigms for improved clinical diagnosis. *Invest Radiol*. 2019;54:383–395.
52. Zijlstra F, Viergever MA, Seevinck PR. Evaluation of variable density and data-driven K-space undersampling for compressed sensing magnetic resonance imaging. *Invest Radiol*. 2016;51:410–419.
53. Khodarahmi I, Fishman EK, Fritz J. Dedicated CT and MRI techniques for the evaluation of the postoperative knee. *Semin Musculoskelet Radiol*. 2018;22:444–456.
54. Khodarahmi I, Fritz J. Advanced MR imaging after total hip arthroplasty: the clinical impact. *Semin Musculoskelet Radiol*. 2017;21:616–629.
55. Khodarahmi I, Nittka M, Fritz J. Leaps in technology: advanced MR imaging after total hip arthroplasty. *Semin Musculoskelet Radiol*. 2017;21:604–615.
56. Vasanawala SS, Alley MT, Hargreaves BA, et al. Improved pediatric MR imaging with compressed sensing. *Radiology*. 2010;256:607–616.
57. Fritz J, Raithel E, Thawait GK, et al. Six-fold acceleration of high-spatial resolution 3D SPACE MRI of the knee through incoherent k-space undersampling and iterative reconstruction-first experience. *Invest Radiol*. 2016;51:400–409.
58. Fritz J, Fritz B, Thawait GK, et al. Advanced metal artifact reduction MRI of metal-on-metal hip resurfacing arthroplasty implants: compressed sensing acceleration enables the time-neutral use of SEMAC. *Skeletal Radiol*. 2016;45:1345–1356.
59. Jungmann PM, Bensler S, Zingg P, et al. Improved visualization of juxtaprosthetic tissue using metal artifact reduction magnetic resonance imaging: experimental and clinical optimization of compressed sensing SEMAC. *Invest Radiol*. 2019;54:23–31.
60. Fritz J, Ahlawat S, Demehri S, et al. Compressed sensing SEMAC: 8-fold accelerated high resolution metal artifact reduction MRI of cobalt-chromium knee arthroplasty implants. *Invest Radiol*. 2016;51:666–676.
61. de Cesar Netto C, Schon LC, da Fonseca LF, et al. Metal artifact reduction MRI for total ankle replacement sagittal balance evaluation. *Foot Ankle Surg*. 2019;25:739–747.
62. de Cesar Netto C, Fonseca LF, Fritz B, et al. Metal artifact reduction MRI of total ankle arthroplasty implants. *Eur Radiol*. 2018;28:2216–2227.
63. Kumar NM, de Cesar Netto C, Schon LC, et al. Metal artifact reduction magnetic resonance imaging around arthroplasty implants: the negative effect of long echo trains on the implant-related artifact. *Invest Radiol*. 2017;52:310–316.
64. Fritz J, Lurie B, Miller TT. Imaging of hip arthroplasty. *Semin Musculoskelet Radiol*. 2013;17:316–327.
65. Khodarahmi I, Isaac A, Fishman EK, et al. Metal about the hip and artifact reduction techniques: from basic concepts to advanced imaging. *Semin Musculoskelet Radiol*. 2019;23:e68–e81.
66. Otazo R, Nittka M, Bruno M, et al. Sparse-SEMAC: rapid and improved SEMAC metal implant imaging using SPARSE-SENSE acceleration. *Magn Reson Med*. 2017;78:79–87.
67. Sutter R, Ulbrich EJ, Jellus V, et al. Reduction of metal artifacts in patients with total hip arthroplasty with slice-encoding metal artifact correction and view-angle tilting MR imaging. *Radiology*. 2012;265:204–214.
68. Runge VM. Current technological advances in magnetic resonance with critical impact for clinical diagnosis and therapy. *Invest Radiol*. 2013;48:869–877.
69. Mugler JP 3rd. Optimized three-dimensional fast-spin-echo MRI. *J Magn Reson Imaging*. 2014;39:745–767.
70. Fritz J, Fritz B, Thawait GG, et al. Three-dimensional CAIPIRINHA SPACE TSE for 5-minute high-resolution MRI of the knee. *Invest Radiol*. 2016;51:609–617.
71. Fritz J, Ahlawat S, Fritz B, et al. 10-min 3D turbo spin echo MRI of the knee in children: arthroscopy-validated accuracy for the diagnosis of internal derangement. *J Magn Reson Imaging*. 2019;49:e139–e151.
72. Shakoor D, Guermazi A, Kijowski R, et al. Cruciate ligament injuries of the knee: a meta-analysis of the diagnostic performance of 3D MRI. *J Magn Reson Imaging*. 2019;50:1545–1560.
73. Shakoor D, Kijowski R, Guermazi A, et al. Diagnosis of knee meniscal injuries by using three-dimensional MRI: a systematic review and meta-analysis of diagnostic performance. *Radiology*. 2019;290:435–445.
74. Shakoor D, Guermazi A, Kijowski R, et al. Diagnostic performance of three-dimensional MRI for depicting cartilage defects in the knee: a meta-analysis. *Radiology*. 2018;289:71–82.
75. Kijowski R, Davis KW, Blankenbaker DG, et al. Evaluation of the menisci of the knee joint using three-dimensional isotropic resolution fast spin-echo imaging: diagnostic performance in 250 patients with surgical correlation. *Skeletal Radiol*. 2012;41:169–178.
76. Kijowski R, Davis KW, Woods MA, et al. Knee joint: comprehensive assessment with 3D isotropic resolution fast spin-echo MR imaging—diagnostic performance compared with that of conventional MR imaging at 3.0 T. *Radiology*. 2009;252:486–495.

77. Kalia V, Fritz B, Johnson R, et al. CAIPIRINHA accelerated SPACE enables 10-min isotropic 3D TSE MRI of the ankle for optimized visualization of curved and oblique ligaments and tendons. *Eur Radiol*. 2017;27:3652–3661.
78. Fritz B, Bensler S, Thawait GK, et al. CAIPIRINHA-accelerated 10-min 3D TSE MRI of the ankle for the diagnosis of painful ankle conditions: performance evaluation in 70 patients. *Eur Radiol*. 2019;29:609–619.
79. Del Grande F, Delcogliano M, Guglielmi R, et al. Fully automated 10-minute 3D CAIPIRINHA SPACE TSE MRI of the knee in adults: a multicenter, multireader, multifield-strength validation study. *Invest Radiol*. 2018;53:689–697.
80. Notohamiprodjo M, Horng A, Pietschmann MF, et al. MRI of the knee at 3T: first clinical results with an isotropic PDfs-weighted 3D-TSE-sequence. *Invest Radiol*. 2009;44:585–597.
81. Notohamiprodjo M, Kuschel B, Horng A, et al. 3D-MRI of the ankle with optimized 3D-SPACE. *Invest Radiol*. 2012;47:231–239.
82. Stern C, Galley J, Frohlich S, et al. Distal femoral cortical irregularity at knee MRI: increased prevalence in youth competitive Alpine skiers. *Radiology*. 2020;296:411–419.
83. Luna R, Fritz J, Del Grande F, et al. Determination of skeletal tumor extent: is an isotropic T1-weighted 3D sequence adequate? *Eur Radiol*. 2021;31:3138–3146.
84. Fayad LM, Parekh VS, de Castro Luna R, et al. A deep learning system for synthetic knee magnetic resonance imaging: is artificial intelligence–based fat-suppressed imaging feasible? *Invest Radiol*. 2021;56:357–368.
85. Van Dyck P, Smekens C, Vanhevel F, et al. Super-resolution magnetic resonance imaging of the knee using 2-dimensional turbo spin echo imaging. *Invest Radiol*. 2020;55:481–493.
86. Kijowski R, Rosas H, Samsonov A, et al. Knee imaging: rapid three-dimensional fast spin-echo using compressed sensing. *J Magn Reson Imaging*. 2017;45:1712–1722.
87. Hilbert T, Schulz J, Marques JP, et al. Fast model-based T_2 mapping using SAR-reduced simultaneous multislice excitation. *Magn Reson Med*. 2019;82:2090–2103.
88. Hilbert T, Sumpf TJ, Weiland E, et al. Accelerated T_2 mapping combining parallel MRI and model-based reconstruction: GRAPPATINI. *J Magn Reson Imaging*. 2018;48:359–368.
89. Raudner M, Schreiner M, Hilbert T, et al. Accelerated T2 mapping of the lumbar intervertebral disc: highly undersampled K-space data for robust T2 relaxation time measurement in clinically feasible acquisition times. *Invest Radiol*. 2020;55:695–701.
90. Fritz J. T2 mapping without additional scan time using synthetic knee MRI. *Radiology*. 2019;293:631–632.
91. Kumar NM, Fritz B, Stern SE, et al. Synthetic MRI of the knee: phantom validation and comparison with conventional MRI. *Radiology*. 2018;289:465–477.
92. Ahlawat S, Morris C, Fayad LM. Three-dimensional volumetric MRI with isotropic resolution: improved speed of acquisition, spatial resolution and assessment of lesion conspicuity in patients with recurrent soft tissue sarcoma. *Skeletal Radiol*. 2016;45:645–652.
93. Pietsch H. Current and future MR contrast agents: seeking a better chemical stability and relaxivity for optimal safety and efficacy. *Invest Radiol*. 2020;55:589–591.
94. Runge VM, Heverhagen JT. Advocating the development of next-generation high-relaxivity gadolinium chelates for clinical magnetic resonance. *Invest Radiol*. 2018;53:381–389.
95. Del Grande F, Santini F, Herzka DA, et al. Fat-suppression techniques for 3-T MR imaging of the musculoskeletal system. *Radiographics*. 2014;34:217–233.
96. Disler DG, McCauley TR, Ratner LM, et al. In-phase and out-of-phase MR imaging of bone marrow: prediction of neoplasia based on the detection of coexistent fat and water. *AJR Am J Roentgenol*. 1997;169:1439–1447.
97. Kumar NM, Ahlawat S, Fayad LM. Chemical shift imaging with in-phase and opposed-phase sequences at 3 T: what is the optimal threshold, measurement method, and diagnostic accuracy for characterizing marrow signal abnormalities? *Skeletal Radiol*. 2018;47:1661–1671.
98. Del Grande F, Subhawong T, Flammang A, et al. Chemical shift imaging at 3 Tesla: effect of echo time on assessing bone marrow abnormalities. *Skeletal Radiol*. 2014;43:1139–1147.
99. Fayad LM, Jacobs MA, Wang X, et al. Musculoskeletal tumors: how to use anatomic, functional, and metabolic MR techniques. *Radiology*. 2012;265:340–356.
100. Bhojwani N, Szpakowski P, Partovi S, et al. Diffusion-weighted imaging in musculoskeletal radiology-clinical applications and future directions. *Quant Imaging Med Surg*. 2015;5:740–753.
101. Schmidt GP, Wintersperger B, Graser A, et al. High-resolution whole-body magnetic resonance imaging applications at 1.5 and 3 Tesla: a comparative study. *Invest Radiol*. 2007;42:449–459.
102. Ahlawat S, Fayad LM, Khan MS, et al. Current whole-body MRI applications in the neurofibromatoses: NF1, NF2, and schwannomatosis. *Neurology*. 2016;87:S31–S39.
103. Ahlawat S, Blakeley JO, Langmead S, et al. Current status and recommendations for imaging in neurofibromatosis type 1, neurofibromatosis type 2, and schwannomatosis. *Skeletal Radiol*. 2020;49:199–219.
104. Consul N, Amini B, Ibarra-Rovira JJ, et al. Li-Fraumeni syndrome and whole-body MRI screening: screening guidelines, imaging features, and impact on patient management. *AJR Am J Roentgenol*. 2021;216:252–263.
105. Hillengass J, Usmani S, Rajkumar SV, et al. International myeloma working group consensus recommendations on imaging in monoclonal plasma cell disorders. *Lancet Oncol*. 2019;20:e302–e312.
106. Fritz J, Tzaribatchev N, Claussen CD, et al. Chronic recurrent multifocal osteomyelitis: comparison of whole-body MR imaging with radiography and correlation with clinical and laboratory data. *Radiology*. 2009;252:842–851.
107. Fritz J. The contributions of whole-body magnetic resonance imaging for the diagnosis and management of chronic recurrent multifocal osteomyelitis. *J Rheumatol*. 2015;42:1359–1360.
108. Fritz J, Tzaribachev N, Thomas C, et al. Magnetic resonance imaging-guided osseous biopsy in children with chronic recurrent multifocal osteomyelitis. *Cardiovasc Intervent Radiol*. 2012;35:146–153.
109. Zhao J, Krug R, Xu D, et al. MRI of the spine: image quality and normal-neoplastic bone marrow contrast at 3 T versus 1.5 T. *AJR Am J Roentgenol*. 2009;192:873–880.
110. Ganesan K, Bydder GM. A prospective comparison study of fast T1 weighted fluid attenuation inversion recovery and T1 weighted turbo spin echo sequence at 3 T in degenerative disease of the cervical spine. *Br J Radiol*. 2014;87:20140091.
111. Liu T, Melkus G, Ramsay T, et al. Bone marrow reconversion with reambulation: a prospective clinical trial. *Invest Radiol*. 2021;56:215–223.
112. Fries P, Runge VM, Kirchin MA, et al. Magnetic resonance imaging of the spine at 3 Tesla. *Semin Musculoskelet Radiol*. 2008;12:238–252.
113. Rodegerdts EA, Boss A, Riemarzik K, et al. 3D imaging of the whole spine at 3T compared to 1.5T: initial experiences. *Acta Radiol*. 2006;47:488–493.
114. Chokshi FH, Sadigh G, Carpenter W, et al. Diagnostic quality of 3D T2-SPACE compared with T2-FSE in the evaluation of cervical spine MRI anatomy. *AJNR Am J Neuroradiol*. 2017;38:846–850.
115. Galley J, Sutter R, Germann C, et al. High-resolution in vivo MR imaging of intraspinal cervical nerve rootlets at 3 and 7 Tesla. *Eur Radiol*. 2021.
116. Ang EC, Robertson AF, Malara FA, et al. Diagnostic accuracy of 3-T magnetic resonance imaging with 3D T1 VIBE versus computer tomography in pars stress fracture of the lumbar spine. *Skeletal Radiol*. 2016;45:1533–1540.
117. Chhabra A, Rozen S, Scott K. Three-dimensional MR neurography of the lumbosacral plexus. *Semin Musculoskelet Radiol*. 2015;19:149–159.
118. Soldatos T, Andreisek G, Thawait GK, et al. High-resolution 3-T MR neurography of the lumbosacral plexus. *Radiographics*. 2013;33:967–987.
119. Fritz J, Ahlawat S. Getting quantitative diffusion-weighted MR neurography and tractography ready for clinical practice. *J Magn Reson Imaging*. 2020;51:1138–1139.
120. Fritz J, Ahlawat S. High-resolution three-dimensional and cinematic rendering MR neurography. *Radiology*. 2018;288:25.
121. Chalian M, Behzadi AH, Williams EH, et al. High-resolution magnetic resonance neurography in upper extremity neuropathy. *Neuroimaging Clin N Am*. 2014;24:109–125.
122. Chhabra A, Chalian M, Soldatos T, et al. 3-T high-resolution MR neurography of sciatic neuropathy. *AJR Am J Roentgenol*. 2012;198:W357–W364.
123. Tagliafico A, Succio G, Emanuele Neumaier C, et al. MR imaging of the brachial plexus: comparison between 1.5-T and 3-T MR imaging: preliminary experience. *Skeletal Radiol*. 2011;40:717–724.
124. Mürtz P, Kaschner M, Lakghomi A, et al. Diffusion-weighted MR neurography of the brachial and lumbosacral plexus: 3.0 T versus 1.5 T imaging. *Eur J Radiol*. 2015;84:696–702.
125. Ahlawat S, Stern SE, Belzberg AJ, et al. High-resolution metal artifact reduction MR imaging of the lumbosacral plexus in patients with metallic implants. *Skeletal Radiol*. 2017;46:897–908.
126. Fritz J, U-Thainual P, Ungi T, et al. Augmented reality visualization using image overlay technology for MR-guided interventions: cadaveric bone biopsy at 1.5 T. *Invest Radiol*. 2013;48:464–470.
127. Lu Y, Fritz J, Li C, et al. Magnetic resonance imaging-guided percutaneous biopsy of mediastinal masses: diagnostic performance and safety. *Invest Radiol*. 2013;48:452–457.
128. Dalili D, Isaac A, Rashidi A, et al. Image-guided sports medicine and musculoskeletal tumor interventions: a patient-centered model. *Semin Musculoskelet Radiol*. 2020;24:290–309.

129. Sequeiros RB, Sinikumpu JJ, Ojala R, et al. Pediatric musculoskeletal interventional MRI. *Top Magn Reson Imaging*. 2018;27:39–44.
130. Fritz J, U-Thainual P, Ungi T, et al. MR-guided vertebroplasty with augmented reality image overlay navigation. *Cardiovasc Intervent Radiol*. 2014;37:1589–1596.
131. Fritz J, U-Thainual P, Ungi T, et al. Augmented reality visualization with use of image overlay technology for MR imaging-guided interventions: assessment of performance in cadaveric shoulder and hip arthrography at 1.5 T. *Radiology*. 2012;265:254–259.
132. Fritz J, U-Thainual P, Ungi T, et al. Augmented reality visualisation using an image overlay system for MR-guided interventions: technical performance of spine injection procedures in human cadavers at 1.5 Tesla. *Eur Radiol*. 2013;23:235–245.
133. Fritz J, Tzaribachev N, Thomas C, et al. Evaluation of MR imaging guided steroid injection of the sacroiliac joints for the treatment of children with refractory enthesitis-related arthritis. *Eur Radiol*. 2011;21:1050–1057.
134. Fritz J, Thomas C, Tzaribachev N, et al. MRI-guided injection procedures of the temporomandibular joints in children and adults: technique, accuracy, and safety. *AJR Am J Roentgenol*. 2009;193:1148–1154.
135. Fritz J, Clasen S, Boss A, et al. Real-time MR fluoroscopy-navigated lumbar facet joint injections: feasibility and technical properties. *Eur Radiol*. 2008;18:1513–1518.
136. Gunaydin I, Pereira PL, Fritz J, et al. Magnetic resonance imaging guided corticosteroid injection of sacroiliac joints in patients with spondylarthropathy. Are multiple injections more beneficial? *Rheumatol Int*. 2006;26:396–400.
137. Fritz J, König CW, Günaydin I, et al. Magnetic resonance imaging–guided corticosteroid-infiltration of the sacroiliac joints: pain therapy of sacroiliitis in patients with ankylosing spondylitis [in German]. *Rofo*. 2005;177:555–563.
138. Fritz J, Bizzell C, Kathuria S, et al. High-resolution magnetic resonance-guided posterior femoral cutaneous nerve blocks. *Skeletal Radiol*. 2013;42:579–586.
139. Fritz J, Dellon AL, Williams EH, et al. Diagnostic accuracy of selective 3-T MR neurography-guided retroperitoneal genitofemoral nerve blocks for the diagnosis of genitofemoral neuralgia. *Radiology*. 2017;285:176–185.
140. Fritz J, Dellon AL, Williams EH, et al. 3-Tesla high-field magnetic resonance neurography for guiding nerve blocks and its role in pain management. *Magn Reson Imaging Clin N Am*. 2015;23:533–545.
141. Fritz J, Thomas C, Clasen S, et al. Freehand real-time MRI-guided lumbar spinal injection procedures at 1.5 T: feasibility, accuracy, and safety. *AJR Am J Roentgenol*. 2009;192:W161–W167.
142. Fritz J, Henes JC, Thomas C, et al. Diagnostic and interventional MRI of the sacroiliac joints using a 1.5-T open-bore magnet: a one-stop-shopping approach. *AJR Am J Roentgenol*. 2008;191:1717–1724.
143. Fritz J, Sonnow L, Morris CD. Adjuvant MRI-guided percutaneous cryoablation treatment for aneurysmal bone cyst. *Skeletal Radiol*. 2019;48:1149–1153.
144. Bonham LW, Phelps A, Rosson GD, et al. MR imaging-guided cryoneurolysis of the sural nerve. *J Vasc Interv Radiol*. 2018;29:1622–1624.
145. Joshi DH, Thawait GK, Del Grande F, et al. MRI-guided cryoablation of the posterior femoral cutaneous nerve for the treatment of neuropathy-mediated sitting pain. *Skeletal Radiol*. 2017;46:983–987.
146. Sonnow L, Gilson WD, Raithel E, et al. Instrument visualization using conventional and compressed sensing SEMAC for interventional MRI at 3T. *J Magn Reson Imaging*. 2018;47:1306–1315.
147. Fritz J, Pereira PL. MR-guided pain therapy: principles and clinical applications [in German]. *Rofo*. 2007;179:914–924.
148. Khodarahmi I, Bonham LW, Weiss CR, et al. Needle heating during interventional magnetic resonance imaging at 1.5- and 3.0-T field strengths. *Invest Radiol*. 2020;55:396–404.
149. Runge VM, Heverhagen JT. Scientific advances, investigative radiology 2020 (and beyond). *Invest Radiol*. 2021;56:271–273.
150. Filli L, Jud L, Luechinger R, et al. Material-dependent implant artifact reduction using SEMAC-VAT and MAVRIC: a prospective MRI phantom study. *Invest Radiol*. 2017;52:381–387.
151. Khodarahmi I, Carrino JA, Fritz J. *Compressed Sensing SEMAC MRI of Hip and Knee Arthroplasty Implants at 1.5T and 3T Field Strengths: An Intra-Subject Comparison Study. 105th Scientific Assembly and Annual Meeting of the Radiological Society of North America (RSNA)*. Chicago, IL: Radiological Society of North America (RSNA); 2019.
152. Khodarahmi I, Kirsch J, Chang G, et al. Metal artifacts of hip arthroplasty implants at 1.5-T and 3.0-T: a closer look into the B1 effects. *Skeletal Radiol*. 2021;50:1007–1015.
153. Bachschmidt TJ, Sutter R, Jakob PM, et al. Knee implant imaging at 3 Tesla using high-bandwidth radiofrequency pulses. *J Magn Reson Imaging*. 2015;41:1570–1580.
154. Khodarahmi I, Rajan S, Sterling R, et al. Heating of hip arthroplasty implants during metal artifact reduction MRI at 1.5- and 3.0-T field strengths. *Invest Radiol*. 2021;56:232–243.